Research Article | Vol. 28, No. 21 / 12 October 2020 / Optics Express 31468
Optics EXPRESS

Second-harmonic generation from subwavelength metal heterodimers

MAYA H. SHOR PELED,[1,4] ESTI TOLEDO,[2,4] SHILPI SHITAL,[1] ACHYUT MAITY,[1] MANDIRA PAL,[1] YONATAN SIVAN,[3] MARK SCHVARTZMAN,[2] AND AVI NIV[1,*]

[1]*Department of Solar Energy and Environmental Physics, Jacob Blaustein Institutes for Desert Research, Ben-Gurion University of the Negev, Sede Boqer Campus, Israel*
[2]*Department of Materials Engineering, Ben-Gurion University, Israel*
[3]*School of Electrical and Computer Engineering, Ben-Gurion University of the Negev, Israel*
[4]*These authors contributed equally*
[*]*aviniv@bgu.ac.il*

Abstract: We experimentally study the optical second-harmonic generation (SHG) from deep subwavelength gold-silver heterodimers, and silver-silver and gold-gold homodimers. Our results indicate a heterodimer SHG that is an order of magnitude more intense than that of the homodimers. In contrast, full-wave calculations that consider the surface and bulk contribution of individual particles, which is the conventional view on such processes, suggest that it is the silver-silver homodimer that should prevail. Based on the deep subwavelength dimension of our structure, we propose that the heterodimer nonlinearity results from a Coulomb interaction between lumped oscillating charges and not from the surface nonlinearity of each particle, as convention would have it. Our proposed model can explain the larger SHG emission observed in gold-silver heterodimers and reproduces its unique spectral lineshape.

1. Introduction

Second-harmonic generation (SHG) is a nonlinear optical (NLO) parametric process where two photons of the pump field produce a single photon at twice the original frequency. While it is forbidden in the bulk of metals, due to their centrosymmetric crystal structure, it is allowed at their interfaces owing to two main inversion-symmetry-violating mechanisms: discontinuity of the screening potential and the finite penetration depth of the electromagnetic field into the metallic domain. The first mechanism spans several angstroms, while the second spans several tens of nanometers at optical frequencies. The two mechanisms are, therefore, known as the *surface* and *bulk* SHG sources of a flat metal surface [1–4]. So far, the source of SHG from small metal spheres and other complex-shaped nanostructures is traditionally attributed to these two mechanisms [5–9]—a paradigm we refer to as the *conventional view* throughout this paper.

Today, second-order processes in isolated particles and dimers [10–13], as well as other geometries [14–17], are well-understood. Relatively little attention, however, has yet been given to heterodimers—dimers constituting particles of different materials [18–22]: Tuan *et al.* studied the SHG from Pt/Cu nanowires and found that the conventional view of SHG could not fully reproduce their experimental findings [23]. Later, Horenber *et al.* observed that Ag-Au heterodimers generate exceptionally strong SHG absent from the Au-Au homodimers [24]. In a more recent publication, Wang *et al.* compared the SHG from Au-Al heterodimers to that of individual Au and Al particles of similar sizes while emphasizing the role of localized plasmon resonances and retardation effects [25]. None of these studies, however, provide detailed explanations for the anomalies that arise in the measured heterodimer's SHG.

In this work, we experimentally and theoretically study SHG from *subwavelength* nanoscaled gold (Au) and silver (Ag) homodimers and heterodimers obtained from an angled deposition

#405247 https://doi.org/10.1364/OE.405247
Journal © 2020 Received 13 Aug 2020; revised 22 Sep 2020; accepted 23 Sep 2020; published 5 Oct 2020

Optics EXPRESS

fabrication approach [26]. This technique produces dimers of particles that are a few tens of nanometers in size and spacing—smaller than what is typically found in the nanoplasmonics literature [8,27–31]. As it turns out, the measured SHG from the heterodimer sample is about an order of magnitude stronger than that of the homodimers, and with a unique spectral lineshape. This outcome is surprising since the conventional theoretical view of SHG predicts that the silver homodimer should have the highest SHG in this case, while displaying a relatively smooth dependence on the pump wavelength in the spectral range of interest. We have thus concluded that the conventional view of metal NLO processes falls short of predicting our heterodimer response.

To resolve this apparent theoretical shortcoming, we have reconsidered the case of the deep subwavelength heterodimer, which led us to adopt a view of two interacting lumped bodies of charge driven by an external pump and with a Coulomb-like interaction between them. While Coulomb interactions are common to nanoscaled optics, they usually involve a linearization that erases any trace of nonlinearity [32,33]. We, however, take a different approach: Since the magnitude of the oscillations is not negligible compared to the size of the system, which by itself is too small for an appreciable phase lag, we take the separation between a fixed number of charges to be the dynamic property. The result is a model with a robust nonlinear character. We show that our model can reproduce both of our unexpected experimental findings—the heterodimer's higher SHG and its distinctive lineshape. We thus conclude that the SHG of our heterodimer comes not from the self-consistent field due to scattering at the fundamental pump frequency and the resulting surface nonlinearity as convention would have it but from the proposed interaction-based NLO mechanism.

In the following, we use experiments, numerical calculations, and the proposed somewhat heuristic analytical model to prove our point. We note that *quantitative* analysis is performed only within the result of each approach. Correspondingly, any comparison across different approaches is made only *qualitatively*. We also note that the purpose of the proposed model is not to replace existing approaches, nor is it to capture all aspects of light-matter interactions in this complicated case. Rather it is meant to deliver a clear view of what is perceived to be the essential feature of the observed reality, which is a new aspect of NLO processes, while ignoring the rest.

2. Background: The conventional view of SHG from metallic structures

The conventional view sees SHG as a linear scattering process from nonlinear sources in the vicinity and on the surface of the metallic domain. The nonlinear sources come from charge oscillations at twice the fundamental frequency (second-harmonic), which may be dipolar or multipolar. The dominant surface contribution is given by [34]:

$$P_i^{2\omega}(\boldsymbol{r}) = \varepsilon_0 \chi_{ijk} E_j(\omega, \boldsymbol{r}_\parallel) E_k(\omega, \boldsymbol{r}_\parallel) \delta(r_\perp - \Sigma) \tag{1}$$

where $\boldsymbol{r} = (\boldsymbol{r}_\parallel, r_\perp)$ is a 3D position vector, χ_{ijk} is a phenomenological second-harmonic surface susceptibility, Σ is the material interface, and ε_0 is the permittivity of vacuum. The linear scattering characteristics of the structure enter the nonlinear sources via $E_k(\omega, r_\parallel)$, the k$^{\text{th}}$ component of the total field (scattered + excitation) at the fundamental frequency ω.

Note that χ_{ijk} is considered here to be a material property that may depend on the pump frequency ω but not on the shape of the scatterer. Therefore, any geometry-related spectral feature of $P_i^{2\omega}$ comes from the field $E_k(\omega, \boldsymbol{r}_\parallel)$. Note that Eq. (1) may also account for the bulk sources of SHG by a proper choice of the susceptibility tensor χ_{ijk} [35–37].

The scattering from the sources of Eq. (1) is, again, a linear process, albeit at twice the fundamental frequency (second-harmonic) that can be described by the following superposition integral:

$$E_j(\boldsymbol{r}_f, 2\omega) = \int_\Sigma G_{ji}(2\omega, \boldsymbol{r}_f, \boldsymbol{r}) P_i^{2\omega}(\boldsymbol{r}) d\boldsymbol{r}. \tag{2}$$

Optics EXPRESS

The ability of the system to convey electromagnetic radiation from a source point on the surface of the metal at location $\boldsymbol{r}$ to the far-field observation point at a location $\boldsymbol{r}_f$ is characterized by the dyad $G_{ji}(2\omega, \boldsymbol{r}_f, \boldsymbol{r})$ that contains all the information about the shape of the scatterer and other boundary conditions [38,39]. The far-field scattering, therefore, also depends on the shape of the scatterer. This shape-dependence may introduce yet another set of spectral features to the scattered SHG at twice the fundamental frequency, in addition to those of the fundamental harmonic self-consistent field $E_k(\omega, r_{\|})$, which may give rise to destructive interference (silencing) or enhancement of the scattered field [16,40].

Given Eqs. (1), (2), we are led to conclude that the spectral lineshape of the SHG results from the combination of two linear scattering processes: first at the fundamental pump frequency through Eq. (1) and later at the second-harmonic frequency through Eq. (2). This well-known fact can be accessed analytically for simple structures such as spheres, rods, or even homodimers, or can be found numerically for more complex shapes [16,41]. It is clear, therefore, that any spectral feature of the SHG that is not due to linear scattering at the fundamental or second-harmonic frequencies cannot result from the conventional view as it is reflected in Eqs. (1), (2).

3. Sample preparation

Fabricating a bi-metal nanostructure is possible by lithographic patterning of each metal; it is, however, extremely challenging due to the required layer alignment. We overcame this obstacle by combining nanoimprint lithography and the double-angle evaporation of two metals [26]. Here, the shadowing effect of the angle evaporation allows the production of metallic heterodimers within a single lithographic cycle. The entire fabrication process is shown in Fig. 1(a). We first

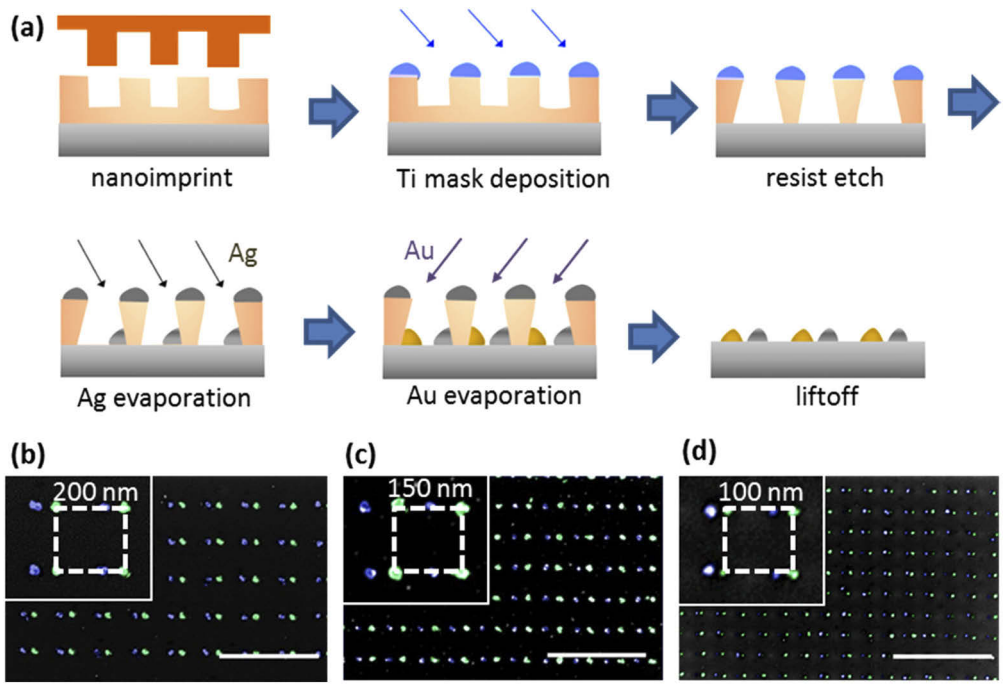

Fig. 1. Sample preparation: (a) Schematic depiction of the fabrication process. (b)–(d) False-colored SEM images of nanofabricated arrays of silver-gold dimers, with densities of 25, 45, and 100 dimers per squared micron, respectively. The scale bar in each image is 500 nm. Insets show a magnified unit-cell of the respective dimer arrays with the corresponding dimensions.

Optics EXPRESS

nanoimprinted a thermal resist on a glass substrate with periodic features of ~20 *nm* in diameter, followed by angle evaporation of the titanium and resist over-etch through the holes formed in the titanium hard-mask using oxygen plasma [42]. We then evaporated two metals at opposite angles and made a resist liftoff process to obtain the dimer arrays. As a final step, the samples were covered with a thick PMMA layer to isolate the small metal particles from the environment and hinder their degradation.

The elegance of this approach is that the nanoimprint mold controlled the dimer density, while the evaporation angle, 35° in our case, determined the spacing within each dimer. The choice of metal at each evaporation step determined if homodimers (Ag-Ag, Au-Au) or heterodimers (Ag-Au) were formed.

We fabricated samples with densities of 25, 45, 100, 200, and 400 dimers per μm^2 on glass substrates. The samples also contained Ag-Ag and Au-Au homodimers arrays identical to the Ag-Au heterodimer in every aspect, except the material composition. Figure 1(b)–(d) shows HR-SEM images of similar samples (on a silicon substrate to enhance the image contrast); the insets show the different unit-cells of the dimer arrays.

4. Experimental results

The SHGs from the Ag-Au heterodimers and Au-Au homodimer arrays at densities of 25, 45, 100, 200, and 400 dimers per μm^2 were measured using the setup illustrated in Fig. 2. A tunable Ti:Sapphire laser with a 150-fs pulse duration at an 80-GHz repetition rate served as the pump (Coherent, Chameleon Ultra II). An optical attenuator (Att) maintained a time-averaged laser power below the sample's damage threshold, a half-wave plate (HWP) aligned the polarization along the dimer's axis, and a Pellin-Broca (PB) prism removed any residual laser luminescence at the designated SHG wavelength. Afterward, the pump beam was expanded and focused onto the sample using a 40X objective (0.66 NA); the resulting spot-size was 875 nm at a wavelength of 800 nm. The SHG from the samples, along with the reflected pump, was collected by the same objective, and a second PB prism removed the pump. Finally, a spectrometer (Andor 303i with iDus UV2 camera) measured the SHG for a pump wavelength ranging from 780–920 nm.

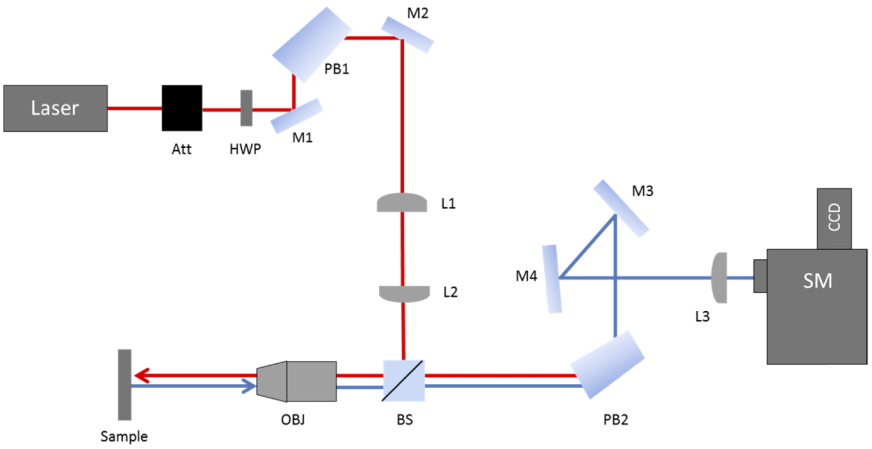

Fig. 2. Schematic depiction of the experimental setup showing the pump laser, attenuator (Att), half-wave plate (HWP), mirrors (M1-M4), lenses (L1-L3), Pellin-Broca prisms (PB1, PB2), objective (OBJ), a beam splitter (BS), and spectrometer (SM) with a CCD camera.

The two PB prisms were realigned at each nominal pump wavelength. The optical path from the beam splitter to the spectrometer was composed of UV grade optical components, and its wavelength-dependent transmission was characterized using a broadband illumination source.

Optics EXPRESS

The raw SHG data was normalized by this transmission function to remove systematic errors from the spectrum. The measured SHG was also corrected for the CCD response based on data from the manufacturer.

The SHG power displayed a quadratic dependence on the pump power, as seen in the Supplement 1. Also, the SHG spectral peak always emerged at half the pump wavelength, and its spectral shape resembled that of the pump at half the width. Therefore, two-photon luminescence from either the Ag or the Au particles, which is characterized by a broader plasmon peak, cannot be the source of the detected signal.

Figure 3(a) shows a typical SHG spectrum from the Ag-Au heterodimer samples for 800 nm pump wavelength. Typical SHG spectra from the Ag-Ag and the Au-Au homodimer are given in Supplement 1. The SHG strength seems to follow a non-monotonic trend: The 25 heterodimers per μm^2 is the weakest, probably due to its low density, the 100 heterodimers per μm^2 is the strongest, and the 200 heterodimers per μm^2 has, once again, weaker SHG. We suspect that this trend is due to inter-dimer interaction in our sample. After all, for the densest sample, the inter- and intra-dimer separations become comparable, which means that the structure becomes more inversion-symmetric even for the case of the heterodimer, which suppresses SHG. In order to assess the role of inter-dimer interaction between the different samples, we show, in Fig. 3(b), the spectra from Fig. 3(a) normalized by the respective sample density. Now, it is seen that the least dense sample has the highest per-heterodimer SHG, while the densest one has the lowest per-heterodimer SHG, thus confirming the detrimental role of inter-dimer interactions in our samples. We, therefore, chose to work with the 100 dimers per μm^2 samples that displayed the correct balance between the total and per-dimer SHG. These samples are dense enough to produce a strong SHG but not too dense to be affected by the inter-dimer interaction and lattice effects.

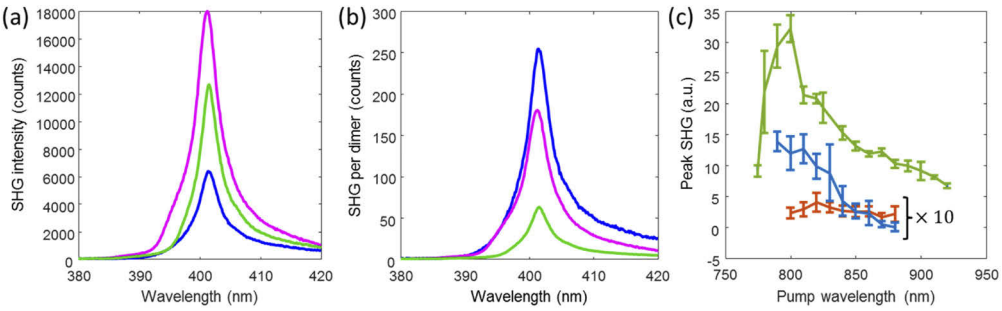

Fig. 3. Typical measured SHG and the corresponding per-heterodimer SHG for the 800-nm pump wavelength in (a) and (b), respectively. The results from the 25, 100, and 200 heterodimers per μm^2 samples are shown in blue, magenta, and green, respectively. (c) Peak SHG as a function of pump wavelength for the Ag-Au heterodimer (green), and the Ag-Ag (blue) and Au-Au (red) homodimers of the 100 dimers per μm^2 samples. The Ag-Ag and Au-Au homodimer responses are multiplied by 10 for better presentation.

Figure 3(c) shows the peak SHG per pump wavelength for the 100 homodimer and heterodimers per μm^2 samples. Error bars show the standard deviation from no less than three independent measurements and, therefore, are indicative of our samples' spatial uniformity. The heterodimer SHG was significantly more substantial than that from the two homodimer samples. Consequently, the homodimer results are shown after being multiplied by 10, for better presentation. Also, the heterodimer displayed a distinct peak, which was absent from the homodimers' response. In what follows, we will compare these two most distinctive characteristics of our samples with simulated results based on the conventional view of SHG and with a proposed electrostatic model tailored to the subwavelength conditions at hand.

Optics EXPRESS

5. Simulation results

We employed the COMSOL finite element solver to account for all aspects of the conventional view of NLO that includes the near-field excitation by linear scattering and the ability of surface sources to scatter SHG to the far-field from Eqs. (1) and (2), respectively. Following a sample geometry characterization procedure (see Supplement 1 for details), we have simulated two hemispherical particles; each is 14 nm in diameter and with centers that are 44 nm apart (30 nm gap). Material data was taken from the literature [43]. The surrounding medium was given a refractive index of 1.5 to account for the glass substrate and the protective PMML cover layer.

Numerical convergence of the SHG calculations was achieved by surrounding a single dimer with spherical shells of perfectly matched layers. Plane-wave excitation polarized along the dimer axis was used at all times. The surface polarization density of the second-harmonic field was calculated for the dominant electric-field component of the single dimer response, which is in the normal direction from the surface [44,45]. The material-dependent value of the relevant susceptibility tensor element was taken from Ref. [7]. Surface discontinuity of the tangential electric field at the metal interface was implemented as a surface magnetic current density [46]. The scattered SH field was calculated using the procedure described in Appendix B of Ref. [46].

This full-wave simulation procedure adequately accounts for all near-field effects, such as localized plasmons [47], multimode interaction [48,49], hybridization [19,32], gap-plasmons [50], cascaded-plasmons [17], the field distribution at the fundamental and second-harmonic frequencies, and the corresponding silencing effects [40].

Figure 4(a) shows the simulated linear scattering cross-section (SCS) of Au-Au and Ag-Ag homodimers and an Ag-Au heterodimer. The homodimers' linear response is dominated by a single resonance, whereas the heterodimer's response is simply the sum of the Ag and the Au particles' responses. The green dashed line shows the simulated SCS (not to scale) of a heterodimer with periodic boundary conditions. The parallelepipedal domain with 100 nm periodicity was used to match the experimental sample. Scattering boundary conditions were used over the domain's top and bottom surfaces. These boundary conditions replaced the spherical domain of the single heterodimer to test the possibility of inter-dimer interactions and lattice effects. The resulting SCS is similar to that of the single heterodimer, indicating that much

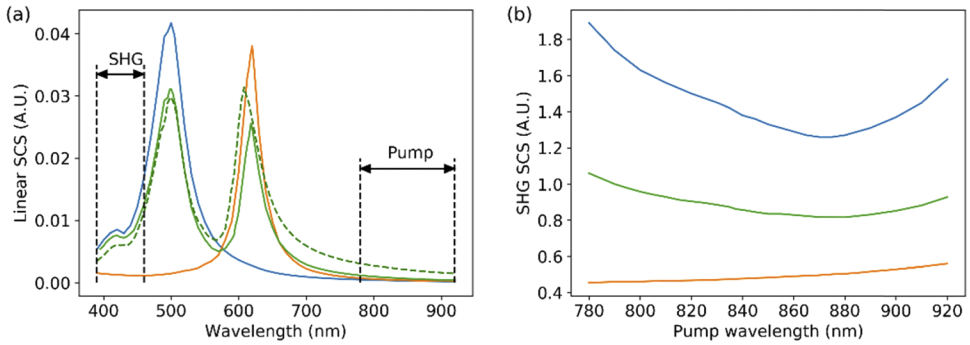

Fig. 4. Simulation results: (a) Normalized scattering cross-section (SCS) of Ag-Ag (blue) and Au-Au (orange) homodimers and the Ag-Au (green) heterodimer. The dashed green line shows the heterodimer CSC that was calculated with periodic boundary conditions. The homodimer cross-section was halved to compensate for the double number of particles of each material relative to the heterodimer case. The spectral ranges of the pump and the corresponding SHG that are relevant for the experimental results are delineated in dashed vertical lines. (b) SCS of the SHG corresponding to the linear-SCS from the solid lines in (a).

Optics EXPRESS

like the experimental case, interdimer interactions and lattice effects are small in the simulation. This observation allows us to calculate the scattered SHG field from the single dimer simulation results.

Figure 4(b) shows SHG SCS for the single dimer results from (a). It is thus evident that, according to the conventional view, it is the Ag-Ag homodimer that has the strongest SHG within the spectral range of interest. The simulation results, therefore, do not reproduce the experimental findings, as they appear in Fig. 3(c). This fact joins past studies that have encountered disagreement between the measured SHG from deep subwavelength metallic systems and the conventional theory [23,26].

6. Proposed electrostatic interaction model

To understand what might have caused the disagreement between the conventional view and the measured homodimer and heterodimer SHG, we need to re-assess the consequences of having a relatively complex deep-subwavelength sized system. After all, the particle size of ~14 nm is comparable to the electromagnetic penetration depth into the respective metals in the frequency range of interest. Therefore, the electromagnetic field in the bulk of the particle is uniform in magnitude and phase, as seen from the simulation results in Supplement 1. As a result, lumped charge oscillations emerge throughout the bulk of the particle [51,52].

The other significant characteristic of the heterodimer is its small inter-particle spacing (~30 nm), leaving no room for appreciable phase retardation at the free-space wavelength of interest, which is greater than 350 nm in this case. The interaction between the lumped oscillating charges is, therefore, electrostatic. In this regime, charge oscillations along the dimer axis, in the different particles composing the dimer, extract a Coulomb force across the dimer gap, which is $\propto \frac{Q_1 Q_2}{D(t)^2}$; namely, the force is proportional to the fixed amounts of lumped charges $Q_1 Q_2$ and inversely proportional to the square of the instantaneous separation between them, $D(t)$. In this case, the nonlinearity of our system results not from the buildup of nonlinear surface polarization in each particle, as the conventional view has it [32,33,53], but from the time-varying denominator of the interaction term. Indeed, for small oscillations, $D(t)^{-2} \propto (1 \pm x(t))^{-2}$ and its power series expansion is $\sum_n (n+1)\, x^n(t)$, which is nonlinear to all orders, not just the second one, due to the presence of the $x^n(t)$ term.

Coupled-oscillator model

Let us consider the system shown in the inset of Fig. 5. Combining the above-mentioned uniform charge oscillations with the particular form of the Coulomb interactions gives the following coupled oscillator model:

$$\begin{cases} \ddot{x} + 2\Gamma_x \dot{x} + \omega_x^2 x = -\frac{e}{m_e} E_P(t) + \frac{k_e e^2 N_y}{m_e} \left[\frac{1}{(D-x)^2} - \frac{1}{(D-x+y)^2} \right] \\ \ddot{y} + 2\Gamma_y \dot{y} + \omega_y^2 y = -\frac{e}{m_e} E_P(t) - \frac{k_e e^2 N_x}{m_e} \left[\frac{1}{(D+y)^2} - \frac{1}{(D+y-x)^2} \right] \end{cases} \tag{3}$$

The dynamic variables x, y denote the instantaneous location of lumped negative charges relative to the static positive ones in each particle. The driving force is $eE_P(t)/m_e$ where $E_P(t)$ is the external pump field, e is the fundamental charge, m_e the electron mass. For the coupling terms, $N_{x,y}$ are the number of charges in each particle and $k_e = \frac{1}{4\pi\varepsilon_0}$ is the Coulomb constant in SI units with ε_0 being the vacuum permittivity. The force between opposite charges within each particle gives the natural frequencies $\omega_{x,y}$, and the corresponding damping is $\Gamma_{x,y}$. Any effect of either the surroundings or the nano-scale confinement on the resonances of the particle enters Eq. (3) through the four phenomenological parameters $\omega_{x,y}$ and $\Gamma_{x,y}$.

There are, however, forces other than the attraction of charges within each particle. These are the electrostatic forces from the lumped charges of the adjacent particle that are given by

Optics EXPRESS

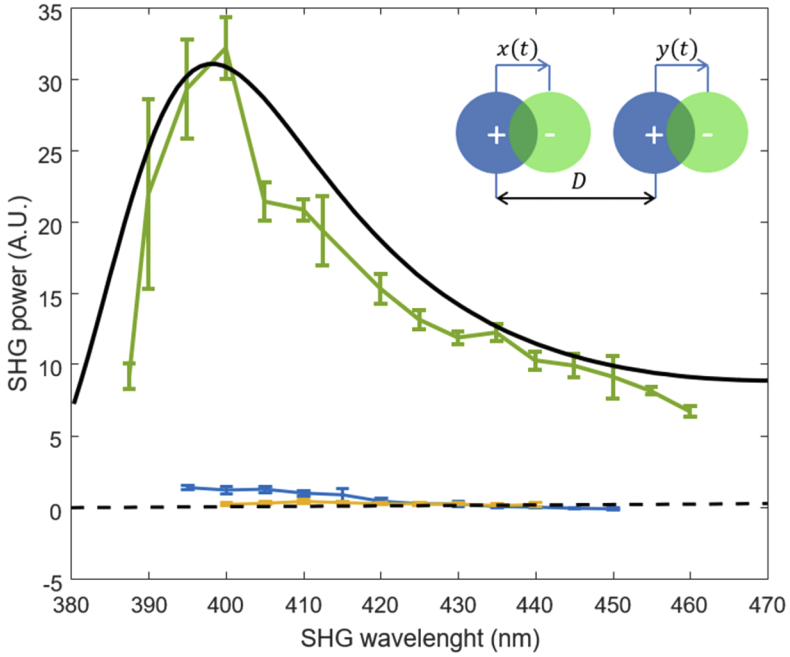

Fig. 5. Calculated (black) and measured (blue) peak SHG of an Ag-Au heterodimer. The orange and yellow lines show the measured homodimers' response. The dashed black line shows the prediction of our model for the homodimer case. Inset shows a schematic depiction of the interacting charges.

the Coulomb force terms in the square brackets of Eq. (3). The first term in each bracket is the attractive interaction with the static positive lumped charge in the opposite particle, and the second is the repulsive force from oscillatory negative lumped charges. The nonlinear characteristic of the dynamic variables x and y comes from these nonlinear coupling terms. It is easy to see that if the separation between particles becomes large, namely $D \rightarrow \infty$, then the model reduces to two uncoupled harmonic oscillators.

Perturbative approximate solution

The proposed dynamic model has an intricate mathematical dependence on its parameters $\omega_{x,y}$, $\Gamma_{x,y}$, $N_{x,y}$, D, and E_p, a comprehensive exploration of which falls outside the scope of this article. Alternatively, we focus on the leading order effect by noting that the charge oscillations x, y are expected to be small compared to the inter-heterodimer spacing D, which allows a series expansion of the coupling term up to its second-order in powers of $\frac{x}{D}$, $\frac{y}{D}$.

We have derived closed-form expressions for the second-harmonic oscillations by assuming a harmonic pump, $E_P = E_0 \sin(\omega t)$, and the following harmonic-series trial solutions: $x = x_0 + x_1 \sin(\omega t + \phi_{x1}) + x_2 \sin(2\omega t + \phi_{x2})$, and $y = y_0 + y_1 \sin(\omega t + \phi_{y1}) + y_2 \sin(2\omega t + \phi_{y2})$. A detailed account of the derivation of the perturbative solution is given in the Supplement 1.

Given that the magnitude and phase of the second-harmonic oscillations are known from the above mentioned perturbative analysis, the induced second-harmonic polarization is given by:

$$P_{2\omega} = N_x e x_2 \cos(\phi_{x2}) + N_y e y_2 \cos(\phi_{y2}), \tag{4}$$

The power of the scattered field, in this case, is proportional to $|P_{2\omega}|^2$ regardless of the multipolar nature of the scattered field from the dimer.

Optics EXPRESS

It can be easily verified that for a homodimer case with $\omega_x = \omega_y$ and $\Gamma_x = \Gamma_y$ the closed-form equations for the second-harmonic charge oscillations gives $x_2 = y_2$ and $\phi_{x2} = \phi_{y2} + \pi$ (after identifying the correct branch of the solution). As a result, $P_{2\omega} \equiv 0$ for the homodimer case, as is required by symmetry considerations, which is how the silencing effect enters our model [8,9,49].

Figure 5 shows the fit of our model to the measured data from Fig. 3(c). The fitting results for the heterodimer and homodimer are shown in solid and dashed black lines, respectively. It is seen that our proposed model captures the essence of our experimental results: The heterodimer SHG is much stronger than the homodimer and with a pronounced spectral peak. Note that the SHG power is plotted as a function of the SHG wavelength in Fig. 5 and not the pump wavelength, as in Fig. 3. Also, the homodimers SHG is shown to scale, which highlights their insignificance relative to the heterodimer.

Fitting was performed for 14 nm particles with a 30 nm gap between them (i.e., $D = 44$ nm). Charge densities were taken as 5.8×10^{28} m^{-3} and 5.9×10^{28} m^{-3} for the Ag and the Au, respectively. The fitting was done manually. It is interesting to note that the fitting resulted in natural frequencies corresponding to 580 nm and 385 nm that are in good agreement with the simulated resonances of the Ag and Au nanoparticles, as shown in Fig. 4(a).

7. Summary and conclusions

It is instructive to compare our results to past studies of homodimer and heterodimer SHG. Tuan *et al.* studied the SHG from 10 nm Pt-Cu wires [23], and their system is, therefore, the two-dimensional equivalent of our case. Accordingly, they found that the result of their full-wave simulation—the conventional view—is not in agreement with their experimental findings in some cases. They attributed this discrepancy to the different work-functions of the metals involved, but they did so only heuristically. The mechanism we propose here may constitute a better description of how material properties relate to the SHG of their sample.

In yet another paper, Ogata *et al.* studied the SHG from Pt nanowires with asymmetric boomerang-shaped cross-sections [26]. They found that significant SHG emerged in some cases where none was expected. Given the deep subwavelength cross-section of the wires, which is ~10 nm, one cannot help but wonder if a mechanism somewhat similar to ours may have prevailed there as well. The asymmetry, in this case, is not due to material heterogeneity but to the asymmetric cross-section of the wire.

Later, Horneber *et al.* and, more recently, also Wang *et al.* have looked at heterodimers but with particles that were larger than the electromagnetic penetration depth into the respective material [24,54]. Accordingly, Wang *et al.* found good agreement between their simulations and their measured data, since the conventional view is perfectly valid in this case. The role played by the compositional asymmetry in their case was, mainly, to diminish the silencing effect (destructive interference) from the far-field scattering of SHG.

It is also worth mentioning that the deep subwavelength size of our system enabled us to forsake the conventional view's field equations of NLO processes in favor of the simpler ordinary differential equations (3). This mechanistic view served us well in demonstrating the source of nonlinearity in our model. It is blind, however, to the multipolar nature of SHG source emissions [49]. A field representation of the proposed interaction-based NLO process should, however, be attainable for simulation procedures that combine the electromagnetic and free-electron field equations (the so-called hydrodynamic model) [55–58]. These advanced schemes could deliver a more comprehensive examination of the near- and far-field spatial distributions in this case. In this regard, we note that the free-electron plasma should be tightly confined to prevent phase mismatch between distinct parts of the dimer that otherwise would eliminate the desired effect. Also, given identically shaped particles, the free-electron plasma should be different in each particle composing the dimer. Finally, our model is not entirely alien to the hydrodynamic model since it is well-known that tightly confined plasma yields an oscillatory behavior [59–61].

Optics EXPRESS

Note, however, that an effective silver-gold heterodimer cannot be achieved based on free-electron oscillations in the visible spectrum due to their almost identical plasma frequencies [62]. The inability of free-electron plasma to support material heterogeneity in the visible spectrum highlights the decisive role that bound-electron oscillations play in our silver-gold heterodimer. Our oscillator-based model possesses a particular strength in this regard by being indifferent to the origin of the resonance, be it free or bound charges.

Regarding the strength of our effect: It cannot be stated that our proposed mechanism is more intense than the bulk and surface sources of the conventional view; a more accurate statement would be that it is more intense for the kind of sample that we used here, namely, deep-subwavelength particles with an asymmetric electrostatic interaction between them. On a general note, we add that the subwavelength dimensions of our sample were deliberately chosen to suppress the conventional SHG as much as possible. Had larger particles were tested, then our sought-after mechanism would weaken at the expense of the conventional surface and bulk sources; it is expected that measurement would be progressively more in agreement with the conventional view as particles become larger

In conclusion, we have found that the measured SHG from the deep subwavelength Ag-Au heterodimer is markedly different from the conventional theory's prediction, which considers effects such as localized plasmons, gap plasmons, and the formation of hot-spots. Re-evaluating the situation led us to propose an electrostatic interaction between the lumped bodies of charges as the source of SHG in our deep subwavelength system. The proposed model successfully reproduced the measured results for the heterodimer and homodimers alike, thus indicating the possibility of a yet unexplored source of optical nonlinearity.

Funding

Israel Science Foundation (152/11, 899/16).

Acknowledgments

Esti Toledo is supported by The Israeli Scholarship Education Foundation (ISEF) for PhD excellence in academic and social leadership. Esti is a fellow of the AdR Women Doctoral Program. The authors extended their gratitude toward Dr. Nireekshan Reddy for his help with SHG simulations.

Disclosures

The authors declare no conflicts of interest.

See Supplement 1 for supporting content.

References

1. N. Bloembergen, R. K. Chang, S. S. Jha, and C. H. Lee, "Optical Second-Harmonic Generation in Reflection from Media with Inversion Symmetry," Phys. Rev. **174**(3), 813–822 (1968).
2. J. Rudnick and E. A. Stern, "Second-harmonic radiation from metal surfaces," Phys. Rev. B **4**(12), 4274–4290 (1971).
3. J. E. Sipe, V. C. Y. So, M. Fukui, and G. I. Stegeman, "Analysis of second-harmonic generation at metal surfaces," Phys. Rev. B **21**(10), 4389–4402 (1980).
4. T. F. Heinz and D. P. DiVincenzo, "Comment on "Forbidden nature of multipolar contributions to second-harmonic generation in isotropic fluids," Phys. Rev. A **42**(10), 6249–6251 (1990).
5. J. I. Dadap, J. Shan, K. B. Eisenthal, and T. F. Heinz, "Second-Harmonic Rayleigh Scattering from a Sphere of Centrosymmetric Material," Phys. Rev. Lett. **83**(20), 4045–4048 (1999).
6. Y. Zeng, W. Hoyer, J. Liu, S. W. Koch, and J. V. Moloney, "Classical theory for second-harmonic generation from metallic nanoparticles," Phys. Rev. B **79**(23), 235109 (2009).

Optics EXPRESS

7. G. Bachelier, J. Butet, I. Russier-Antoine, C. Jonin, E. Benichou, and P.-F. F. Brevet, "Origin of optical second-harmonic generation in spherical gold nanoparticles: Local surface and nonlocal bulk contributions," Phys. Rev. B: Condens. Matter Mater. Phys. **82**(23), 235403 (2010).
8. J. Butet, P.-F. Brevet, and O. J. F. Martin, "Optical Second Harmonic Generation in Plasmonic Nanostructures: From Fundamental Principles to Advanced Applications," ACS Nano **9**(11), 10545–10562 (2015).
9. K. O'Brien, H. Suchowski, J. Rho, A. Salandrino, B. Kante, X. Yin, and X. Zhang, "Predicting nonlinear properties of metamaterials from the linear response," Nat. Mater. **14**(4), 379–383 (2015).
10. J. Shan, J. I. Dadap, I. Stiopkin, G. A. Reider, and T. F. Heinz, "Experimental study of optical second-harmonic scattering from spherical nanoparticles," Phys. Rev. A: At., Mol., Opt. Phys. **73**(2), 023819 (2006).
11. J. Nappa, I. Russier-Antoine, E. Benichou, C. Jonin, and P. F. Brevet, "Second harmonic generation from small gold metallic particles: From the dipolar to the quadrupolar response," J. Chem. Phys. **125**(18), 184712 (2006).
12. B. K. Canfield, H. Husu, J. Laukkanen, B. Bai, M. Kuittinen, J. Turunen, and M. Kauranen, "Local field asymmetry drives second-harmonic generation in noncentrosymmetric nanodimers," Nano Lett. **7**(5), 1251–1255 (2007).
13. C. Awada, F. Kessi, C. Jonin, P. M. Adam, S. Kostcheev, R. Bachelot, P. Royer, I. Russier-Antoine, E. Benichou, G. Bachelier, and P. F. Brevet, "On- and off-axis second harmonic generation from an array of gold metallic nanocylinders," J. Appl. Phys. **110**(2), 023109 (2011).
14. J. A. H. Van Nieuwstadt, M. Sandtke, R. H. Harmsen, F. B. Segerink, J. C. Prangsma, S. Enoch, and L. Kuipers, "Strong modification of the nonlinear optical response of metallic subwavelength hole arrays," Phys. Rev. Lett. **97**(14), 146102 (2006).
15. A. Salomon, Y. Prior, M. Fedoruk, J. Feldmann, R. Kolkowski, and J. Zyss, "Plasmonic coupling between metallic nanocavities," J. Opt. **16**(11), 114012 (2014).
16. K. Nireekshan Reddy, P. Y. Chen, A. I. Fernández-Domínguez, and Y. Sivan, "Surface second-harmonic generation from metallic-nanoparticle configurations: A transformation-optics approach," Phys. Rev. B **99**(23), 235429 (2019).
17. K. Li, M. I. Stockman, and D. J. Bergman, "Enhanced second harmonic generation in a self-similar chain of metal nanospheres," Phys. Rev. B: Condens. Matter Mater. Phys. **72**(15), 153401 (2005).
18. A. Lombardi, M. P. Grzelczak, A. Crut, P. Maioli, I. Pastoriza-Santos, L. M. Liz-Marzán, N. Del Fatti, and F. Vallée, "Optical Response of Individual Au–Ag@SiO 2 Heterodimers," ACS Nano **7**(3), 2522–2531 (2013).
19. S. Sheikholeslami, Y. W. Jun, P. K. Jain, and A. P. Alivisatos, "Coupling of optical resonances in a compositionally asymmetric plasmonic nanoparticle dimer - supporting information," Nano Lett. **10**(7), 2655–2660 (2010).
20. G. Bachelier, I. Russier-Antoine, E. Benichou, C. Jonin, N. Del Fatti, F. Vallee, and P. F. Brevet, "Fano profiles induced by near-field coupling in heterogeneous dimers of gold and silver nanoparticles," Phys. Rev. Lett. **101**(19), 197401 (2008).
21. E. R. Encina and E. A. Coronado, "On the far field optical properties of Ag-Au nanosphere pairs," J. Phys. Chem. C **114**(39), 16278–16284 (2010).
22. O. Peña-Rodríguez, U. Pal, M. Campoy-Quiles, L. Rodríguez-Fernández, M. Garriga, and M. I. Alonso, "Enhanced Fano resonance in asymmetrical Au:Ag heterodimers," J. Phys. Chem. C **115**(14), 6410–6414 (2011).
23. N. A. Tuan and G. Mizutani, "Metal-interface second harmonic generation from Pt/Cu bimetallic nanowire arrays on NaCl(110) faceted templates," e-J. Surf. Sci. Nanotechnol. **7**, 831–835 (2009).
24. A. Horneber, A.-L. Baudrion, P.-M. Adam, A. J. Meixner, and D. Zhang, "Compositional-asymmetry influenced non-linear optical processes of plasmonic nanoparticle dimers," Phys. Chem. Chem. Phys. **15**(21), 8031 (2013).
25. J. Wang, J. Butet, G. D. Bernasconi, A. L. Baudrion, G. Lévêque, A. Horrer, A. Horneber, O. J. F. Martin, A. J. Meixner, M. Fleischer, P. M. Adam, and D. Zhang, "Strong second-harmonic generation from Au-Al heterodimers," Nanoscale **11**(48), 23475–23481 (2019).
26. Y. Ogata, N. Anh Tuan, Y. Miyauchi, and G. Mizutani, "Optical second harmonic generation from Pt nanowires with boomerang-like cross-sectional shapes," J. Appl. Phys. **110**(4), 044301 (2011).
27. J. A. Schuller, E. S. Barnard, W. Cai, Y. C. Jun, J. S. White, and M. L. Brongersma, "Plasmonics for extreme light concentration and manipulation," Nat. Mater. **9**(3), 193–204 (2010).
28. M. I. Stockman, K. Kneipp, S. I. Bozhevolnyi, S. Saha, A. Dutta, J. Ndukaife, N. Kinsey, H. Reddy, U. Guler, V. M. Shalaev, A. Boltasseva, B. Gholipour, H. N. S. Krishnamoorthy, K. F. MacDonald, C. Soci, N. I. Zheludev, V. Savinov, R. Singh, P. Groß, C. Lienau, M. Vadai, M. L. Solomon, D. R. Barton, M. Lawrence, J. A. Dionne, S. V. Boriskina, R. Esteban, J. Aizpurua, X. Zhang, S. Yang, D. Wang, W. Wang, T. W. Odom, N. Accanto, P. M. de Roque, I. M. Hancu, L. Piatkowski, N. F. van Hulst, and M. F. Kling, "Roadmap on plasmonics," J. Opt. **20**(4), 043001 (2018).
29. M. Kauranen and A. V. Zayats, "Nonlinear plasmonics," Nat. Photonics **6**(11), 737–748 (2012).
30. A. Capretti, E. F. Pecora, C. Forestiere, L. Dal Negro, and G. Miano, "Size-dependent second-harmonic generation from gold nanoparticles," Phys. Rev. B: Condens. Matter Mater. Phys. **89**(12), 125414 (2014).
31. N. C. Panoiu, W. E. I. Sha, D. Y. Lei, and G. C. Li, "Nonlinear optics in plasmonic nanostructures," J. Opt. (Bristol, U. K.) **20**(8), 083001 (2018).
32. P. Nordlander, C. Oubre, E. Prodan, K. Li, and M. I. Stockman, "Plasmon hybridization in nanoparticle dimers," Nano Lett. **4**(5), 899–903 (2004).
33. Q. Hu, D. Jin, S. H. Nam, J. Xiao, Y. Liu, X. Zhang, and N. X. Fang, "Ultrafast fluorescent decay induced by metal-mediated dipole-dipole interaction in two-dimensional molecular aggregates," Proc. Natl. Acad. Sci. U. S. A. **114**(38), 10017–10022 (2017).

Optics EXPRESS

34. T. F. Heinz, "Second-Order Nonlinear Optical Effects at Surfaces and Interfaces," Mod. Probl. Condens. Matter Sci. **29**, 353–416 (1991).
35. E. Sipe, V. Mizrahi, G. I. Stegeman, J. E. Sipe, V. Mizrahi, and G. I. Stegeman, "Fundamental difficulty in the use of second-harmonic generation as a strictly surface probe," Phys. Rev. B **35**(17), 9091–9094 (1987).
36. C. Ciracì, E. Poutrina, M. Scalora, and D. R. Smith, "Second-harmonic generation in metallic nanoparticles: Clarification of the role of the surface," Phys. Rev. B: Condens. Matter Mater. Phys. **86**(11), 115451 (2012).
37. C. Forestiere, A. Capretti, and G. Miano, "Surface integral method for second harmonic generation in metal nanoparticles including both local-surface and nonlocal-bulk sources," J. Opt. Soc. Am. B **30**(9), 2355 (2013).
38. M. Born and E. Wolf, *Principles of Optics*, Seventh ed (Cambridge University Press, 1999).
39. J. D. Jackson, *Classical Electrodynamics*, 3rd ed. (John Wiley & Sons, 1998).
40. J. Berthelot, G. Bachelier, M. Song, P. Rai, G. Colas des Francs, A. Dereux, and A. Bouhelier, "Silencing and enhancement of second-harmonic generation in optical gap antennas," Opt. Express **20**(10), 10498 (2012).
41. J. I. Dadap, J. Shan, and T. F. Heinz, "Theory of optical second-harmonic generation from a sphere of centrosymmetric material: small-particle limit," J. Opt. Soc. Am. B **21**(7), 1328–1347 (2004).
42. M. Schvartzman and S. J. Wind, "Robust pattern transfer of nanoimprinted features for sub-5-nm fabrication," Nano Lett. **9**(10), 3629–3634 (2009).
43. E. D. Palik, *Handbook of Optical Constants of Solids* (Academic Press, 1998), Vol. 1.
44. F. X. Wang, F. J. Rodríguez, W. M. Albers, R. Ahorinta, J. E. Sipe, and M. Kauranen, "Surface and bulk contributions to the second-order nonlinear optical response of a gold film," Phys. Rev. B **80**(23), 233402 (2009).
45. J. Wang, J. Jéré, J. Butet, A.-L. Baudrion, A. Horrer, G. Lévêque, O. J. F. Martin, A. J. Meixner, M. Fleischer, P.-M. Adam, A. Horneber, and D. Zhang, "Direct Comparison of Second Harmonic Generation and Two-Photon Photoluminescence from Single Connected Gold Nanodimers," J. Phys. Chem. C **120**(31), 17699–17710 (2016).
46. K. N. Reddy, P. Y. Chen, A. I. Fernández-Domínguez, and Y. Sivan, "Revisiting the boundary conditions for second-harmonic generation at metal-dielectric interfaces," J. Opt. Soc. Am. B **34**(9), 1824–1832 (2017).
47. L. Michaeli, S. Keren-Zur, O. Avayu, H. Suchowski, and T. Ellenbogen, "Nonlinear Surface Lattice Resonance in Plasmonic Nanoparticle Arrays," Phys. Rev. Lett. **118**(24), 243904 (2017).
48. M. Celebrano, X. Wu, M. Baselli, S. Großmann, P. Biagioni, A. Locatelli, C. De Angelis, G. Cerullo, R. Osellame, B. Hecht, L. Duò, F. Ciccacci, and M. Finazzi, "Mode matching in multiresonant plasmonic nanoantennas for enhanced second harmonic generation," Nat. Nanotechnol. **10**(5), 412–417 (2015).
49. G. D. Bernasconi, J. Butet, and O. J. F. Martin, "Mode analysis of second-harmonic generation in plasmonic nanostructures," J. Opt. Soc. Am. B **33**(4), 768 (2016).
50. Z. Dong, M. Asbahi, J. Lin, D. Zhu, Y. M. Wang, K. Hippalgaonkar, H. S. Chu, W. P. Goh, F. Wang, Z. Huang, and J. K. W. Yang, "Second-Harmonic Generation from Sub-5 nm Gaps by Directed Self-Assembly of Nanoparticles onto Template-Stripped Gold Substrates," Nano Lett. **15**(9), 5976–5981 (2015).
51. E. Prodan, C. Radloff, N. J. Halas, and P. Nordlander, "A hybridization model for the plasmon response of complex nanostructures," Science **302**(5644), 419–422 (2003).
52. B. Metzger, L. Gui, J. Fuchs, D. Floess, M. Hentschel, and H. Giessen, "Strong Enhancement of Second Harmonic Emission by Plasmonic Resonances at the Second Harmonic Wavelength," Nano Lett. **15**(6), 3917–3922 (2015).
53. N. Liver, A. Nitzan, and K. F. Freed, "Radiative and nonradiative decay rates of molecules adsorbed on clusters of small dielectric particles," J. Chem. Phys. **82**(8), 3831–3840 (1985).
54. J. Wang, J. Butet, G. D. Bernasconi, A. L. Baudrion, G. Lévêque, A. Horrer, A. Horneber, O. J. F. Martin, A. J. Meixner, M. Fleischer, P. M. Adam, and D. Zhang, "Strong second-harmonic generation from Au–Al heterodimers - Supporting Information," Nanoscale **11**(48), 23475–23481 (2019).
55. P. Ginzburg, A. V. Krasavin, G. A. Wurtz, and A. V. Zayats, "Nonperturbative hydrodynamic model for multiple harmonics generation in metallic nanostructures," ACS Photonics **2**(1), 8–13 (2015).
56. G. Toscano, J. Straubel, A. Kwiatkowski, C. Rockstuhl, F. Evers, H. Xu, N. A. Mortensen, and M. Wubs, "Resonance shifts and spill-out effects in self-consistent hydrodynamic nanoplasmonics," Nat. Commun. **6**(1), 7132 (2015).
57. C. Ciracì, "Current-dependent potential for nonlocal absorption in quantum hydrodynamic theory," Phys. Rev. B **95**(24), 245434 (2017).
58. S. Sideris and T. Ellenbogen, "Terahertz generation in parallel plate waveguides activated by nonlinear metasurfaces," Opt. Lett. **44**(14), 3590 (2019).
59. P. B. Parks, T. E. Cowan, R. B. Stephens, and E. M. Campbell, "Model of neutron-production rates from femtosecond-laser–cluster interactions," Phys. Rev. A **63**(6), 063203 (2001).
60. S. V. Fomichev, S. V. Popruzhenko, D. F. Zaretsky, and W. Becker, "Laser-induced nonlinear excitation of collective electron motion in a cluster," J. Phys. B: At., Mol. Opt. Phys. **36**(18), 3817–3834 (2003).
61. P. M. Tomchuk and D. V. Butenko, "Nonlinear plasma dipole oscillations in spheroidal metal nanoparticles," Ukr. J. Phys. **56**, 1110–1119 (2011).
62. N. W. Ashcroft and N. D. Mermin, *Solid State Physics* (Brooks/Cole, 1976).